A study of nucleating flow of steam in a cascade of supersonic blading by the time-marching method

F. Bakhtar* and K. S. So†

* School of Manufacturing and Mechanical Engineering, University of Birmingham, Birmingham, UK

† Yamazaki Machine Tool Company, Warndon, Worcester, UK; formerly of University of Birmingham

A treatment of a blade-to-blade flow of nucleating steam in a cascade of supersonic tip section blading by the time-marching method is presented. To reduce the numerical errors associated with the method, an auxiliary mesh is embedded in selected areas of the field thereby increasing the accuracy. The agreement obtained between the solutions and the available experimental results is reasonable.

Keywords: nucleation; steam turbines; fluid dynamics; time-marching; two-phase-flow

Introduction

This investigation follows an earlier one in which a case of two-dimensional (2-D) nucleating flow of steam in a cascade of supersonic tip section blading was treated by the time-marching method.[1] During the expansion of steam through turbines, the state path crosses the saturation line, and the fluid first supercools and then nucleates to become a two-phase mixture. The formation and subsequent behavior of the liquid create problems that lead to losses of performance in the wet stages, but the detailed mechanisms that give rise to them are insufficiently understood. Because of the dominant role played by steam turbines in the generation of electric power, any progress in understanding leading to an improvement in efficiency will yield handsome savings in fuel costs.

The development of nucleation theory has been of help to the study of wetness problems in steam turbines, as in combination with the gas dynamic equations it allows nucleating and wet steam flows to be described analytically. In the earlier stages of the development of the subject, the investigations were confined to one-dimensional (1-D) flows. A substantial body of experience is now available to demonstrate that treatments based on this approach predict the 1-D flows of nucleating steam with reasonable accuracy. However, in order to apply such a treatment to the flow in the wet stages of steam turbines it is desirable to extend the method to 2-D and three-dimensional (3-D) fields. In these problems however, the flows are generally transonic with appreciable supersonic zones, while the speed of sound in such mixtures is not explicit and depends on local conditions. Under these circumstances, the most suitable method of treating the equations is the time-marching technique, and a development based on Denton's technique[2] resulted in a successful solution.[3] In the investigation cited, comparisons with measurements in nozzles showed reasonable agreement. However, when the treatment was applied to a case of 2-D blade-to-blade flow, although important differences were predicted between superheated and nucleating solutions, the findings could not be checked against experimental measurements due to lack of direct observations. This was because without the availability of a supply of supercooled steam it is not practicable to achieve substantial homogeneous nucleation of steam in subsonic flows, and the blade profiles examined were those of converging nozzles.

Two-dimensional two-phase flows of steam can, however, be observed in cascades of supersonic tip section blading and a number of unpublished such measurements were made available to the group at Birmingham. Thus despite the numerical difficulties associated with the particular configuration, solution of the flow was attempted in the earlier investigation. It was found that the solutions were affected by the numerical errors associated with the time-marching technique and to obtain adequate agreement with the observed pressure distributions the flow inlet angle had to be reduced by 1.8°. An important factor in two-phase flows is the local rate of phase change, which is sensitive to the degree of superheating or supercooling of the fluid and is affected by numerical errors. To obtain a more satisfactory solution it has been necessary to seek means of reducing numerical errors. The remedy adopted has consisted of embedding a finer mesh in the computational grid where the errors are generated. The results of the investigation form the subject of this article.

Outline of the treatment

The governing equations are the conservation equations of mass, momentum, and energy written for a two-phase mixture, which are then combined with the equations describing interphase mass and heat transfer. In the present application, because of the smallness of the droplets, interphase slip is regarded as negligible. In addition, because of the accelerating nature of the flow, the boundary layers containing any viscous shearing are assumed to be thin, and the external heat exchange has been regarded as small. Thus the bulk of the flow has been assumed to be inviscid.

The method of treatment is essentially that described in Reference 3, but its basic time-marching algorithm has been modified in accordance with Denton's improved technique.[4] A brief summary of the main features of the method is given in Appendix (1).

The experimental observations consist of surface pressure measurements carried out in the cascade at the same pressure levels but at two different inlet temperatures. In one family,

Address reprint requests to Dr. Bakhtar at the School of Manufacturing and Mechanical Engineering, University of Birmingham, P.O. Box 363, Birmingham B15 2TT, UK.

Received 3 January 1989; accepted 30 July 1990.

designated as dry tests, the inlet temperature has been sufficiently high to inhibit nucleation. In the second, referred to as wet tests, the inlet temperature has been lowered and steam allowed to nucleate within the blades. In addition Schlieren photographs of dry and wet tests have also been recorded. Relevant information about these results is given in Reference 1. However, before describing the application of the treatment to the condensing flow, it is convenient to consider its application to the dry test. This will allow for the selection of the grid without the additional complication of the two-phase effects.

Mesh arrangement

The general arrangement of the standard mesh relative to the blade profile is shown in Figure 1a, and an enlarged view of a slightly changed computational grid in the vicinity of the leading edge is shown in Figure 1b. It will be noted that with the standard mesh the shape of the blade nose would be distorted. This is a consequence of the inlet geometry and the need to make the x axis coincident with the axial direction, in order for the periodicity condition particularly downstream of the trailing edge in nucleating flows to be more easily enforced. This makes it difficult to model the flow round the leading edge accurately. Numerical errors resulting from an unsatisfactory representation will spread throughout the whole flow field and make the solution inaccurate.

It was thought possible to overcome this difficulty by treating the flow round the leading edge separately from the remainder of the field. This can be done by embedding a patch within the main computational grid. The details of the arrangement adopted and the procedure used are given in Appendix 2.

Application to the dry test

The main grid originally adopted consisted of 28×66 mesh points, with the stations evenly spaced in the axial direction and the mesh extended only half an axial chord length upstream and downstream of the blade. The embedded grid used with this arrangement is in fact that shown in Figure A.2. The solutions carried out in conjunction with this are referred to as solutions 1. The surface pressure distributions resulting from the application of this arrangement to the fully loaded dry test are compared with the measurements in Figure 2a. To provide comparison, the resulting distributions from a standard solution are shown as an inset to Figure 2a. The differences between the local values of stagnation pressure and the upstream value were used for evaluating the quality of the solutions. Although with the introduction of the embedded mesh the agreement

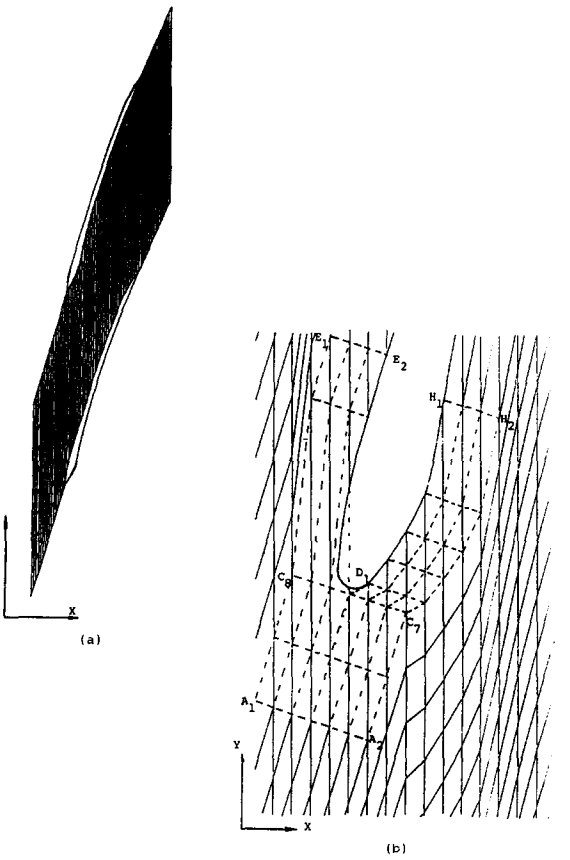

Figure 1 Computational grid: (a) general arrangement of standard mesh; (b) enlarged view of mesh in the vicinity of the leading edge

with the surface pressure distributions and the modeling of the flow around the leading edge has improved considerably, numerical errors were not completely eliminated. Furthermore, although the surface pressure distributions for the flow inlet angle of 72.8° showed reasonable agreement with the measurements, the resulting distributions did not appear realistic when the inlet angle was altered. Further investigation showed the problems to be caused by the change in the blade curvature near the leading edge of the suction surface.

To deal with the situation the embedded mesh was extended farther downstream of the leading edge on the suction surface, and the spacing of the elements of the embedded mesh in the tangential direction was reduced by a factor of 4. At this stage the main grid itself was extended to a whole axial chord upstream and downstream of the blade, and with reference to

Notation

B	Second virial coefficient
CF	Correction factor
h	Specific enthalpy
N	Number of droplets per unit mass
p	Pressure
R	Gas constant
r	Droplet radius
s	Control volume surface
T	Temperature
t	Time
V	Volume
w	Wetness fraction
x, y	Cartesian coordinates
u, v	Components of velocity in x and y directions

Greek characters

ρ	Density

Subscripts

G	Vapor phase
L	Liquid phase
O	Stagnation conditions
x, y	Projections in coordinate directions

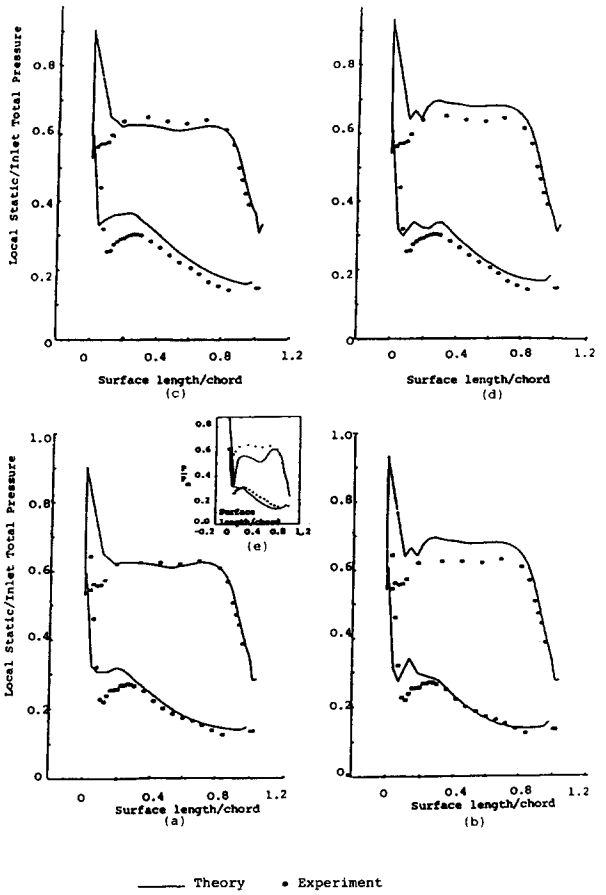

Figure 2 Comparison of theoretical and experimental surface pressure distributions: (a) dry test solution 1; (b) dry test solution 2; (c) wet test solution 1; (d) wet test solution 2; (e) dry test standard solution

Equation A.11 second-order terms were introduced into the solutions by setting the value of G equal to unity in the embedded grid. This reduced the numerical errors further. Solutions obtained with this arrangement are referred to as solutions 2. The surface pressure distributions resulting from the application of this arrangement to the fully loaded dry test are compared with the observations in Figure 2b. With the reduction of the errors the agreement between the theoretical and experimental results improved on the suction surface, but the agreement on the pressure surface was less satisfactory. On the other hand changes in inlet flow angle gave solutions that seemed realistic.

Application to nucleating conditions

Influence of the accumulated numerical errors

In the range of conditions considered, a 1% change in the stagnation pressure caused by the numerical errors corresponds approximately to a 1°C change in the fluid temperature. Consequently, in the region where the steam is supercooled but still dry, this corresponds with a 1°C change in supercooling. Errors of a few degrees in the fluid temperatures have the greatest effect in the region of the Wilson point, as they can influence the nucleation rate drastically. The variations in these errors as measured by percentage changes in stagnation pressure along the quasi-streamlines for solution 2 are shown in Figure 3. The numbers along the curves refer to the position of the quasi-streamlines in the tangential direction. The broken line indicates the position of the onset of nucleation in the solution. The leading and trailing edges are at stations 34 and 65, respectively. The accumulated errors are comparatively high in the nucleation zone near the suction surface, but they are quite low in the core of the flow.

Surface pressure distributions

The experimental surface pressure distributions observed in wet and dry tests are compared in Figure 4a. A similar comparison for the results of solution 2 is shown in Figure 4b. The difference between the measurements is particularly noticeable on the

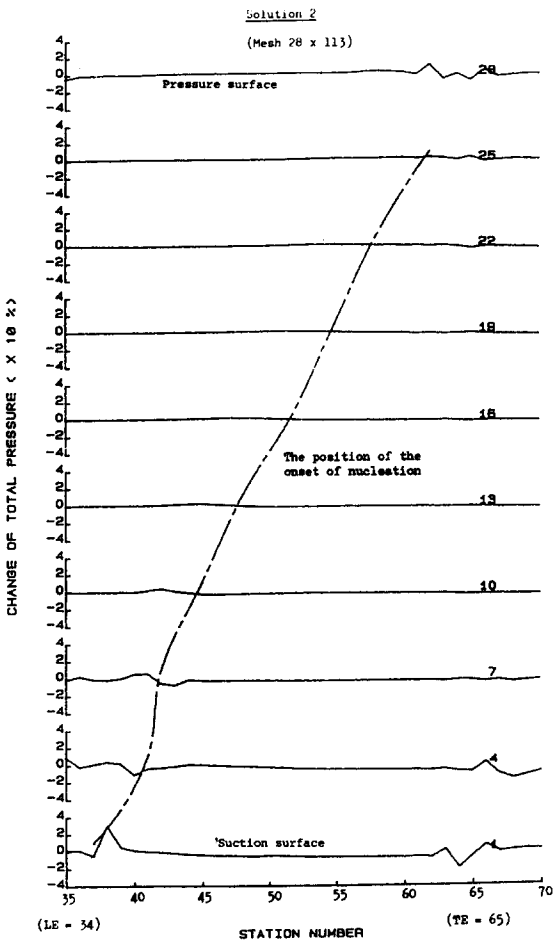

Figure 3 Behavior of numerical errors in solution 2

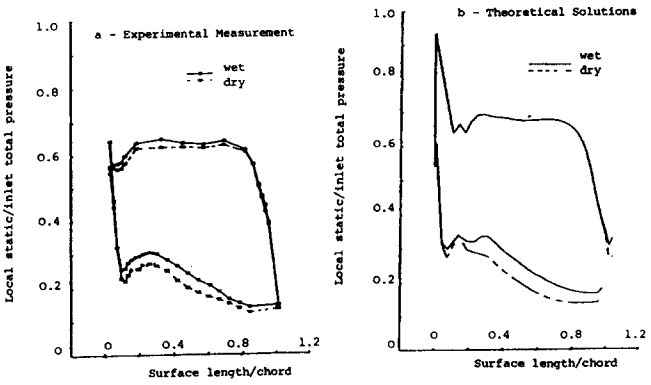

Figure 4 Comparison of dry and wet surface pressure distributions

suction surface. The overall effect is a reduction in the area enclosed by the curves, which will be experienced as a loss of output due to the condition of the fluid. But this does not necessarily correspond with a loss of efficiency.

The comparisons between calculated and experimental results for the wet test for solutions (1) and (2) are shown in Figures 2c and 2d, respectively. The agreement between solution 2 and the experimental results is particularly good on the suction surface. The theoretical curve has the right trend at the leading edge. The sudden rise of pressure is a consequence of the sudden change of curvature near the throat on this surface and is caused by numerical errors. This could have been improved by further refinement of the grid but was not regarded as justified. The reason for the discrepancy between the experimental and theoretical results on the pressure surface is not known. As seen from Figure 3, numerical errors are negligible on the pressure surface, and Schlieren photographs do not show any particular boundary-layer problems.

In the actual calculations, the converged solution (2) was stable. In contrast solution (1) showed some instability downstream of the throat in the wet solution, which corresponded with the thermodynamic instability in condensing flows discussed, among others, in Reference 5. However, as the high-speed film records taken during the tests were not kept, this could not be checked against direct observations.

Behavior of other flow properties

The variations of wetness fraction and Mach number across the flow field for solution (2) for the wet test are given in Figure 5. For comparison, the variations in Mach number for the dry solution are also given. The sonic lines appear at the throat position for both the dry and wet solutions. The overall Mach numbers are lower for the wet flow, which is retarded by the addition of heat released by condensation. The suction side trailing edge shocks can also be seen from these distributions. These are located just downstream of the constant Mach number line 2 in the dry solution and 1.6 in the wet solution. The wetness fraction decreases after the shock because of evaporation.

It will also be noted that the wetness fractions and Mach numbers on either side of the periodic boundary downstream of the trailing edge are very different. This is caused by the different thermodynamic paths followed by the fluid reaching the trailing edge from the two sides of the blade.

The variations in the degrees of supercooling, nucleation rate, and droplet sizes along four quasi-stream lines resulting from theoretical solutions are shown in Figure 6. The numbers along the curves indicate the position of the quasi-streamlines in the tangential direction. Although the flow nucleates earlier near the suction surface, the variations of the parameters describing the reversion of the fluid are surprisingly uniform across the passage. The change in the maximum value of the nucleation rate is less than one order of magnitude. As the resulting droplet sizes are expected to vary with the cube root of the nucleation rate, these variations are relatively small. This can be seen from the resulting droplet sizes, which are of the order of 0.01 μm in radius, and the maximum variation across the section is only a factor of 2. No measurements of droplet sizes in cascades are yet available to compare with the predicted values, but these estimates are comparable with sizes expected in convergent–divergent nozzles. Indeed, as the particular profile section studied contains a fair divergent section, larger droplets can only be nucleated if the inlet temperature were raised sufficiently to move the Wilson point downstream to a location where the rate of expansion is low. After the formation of the droplets, there is a period of very rapid growth during which the

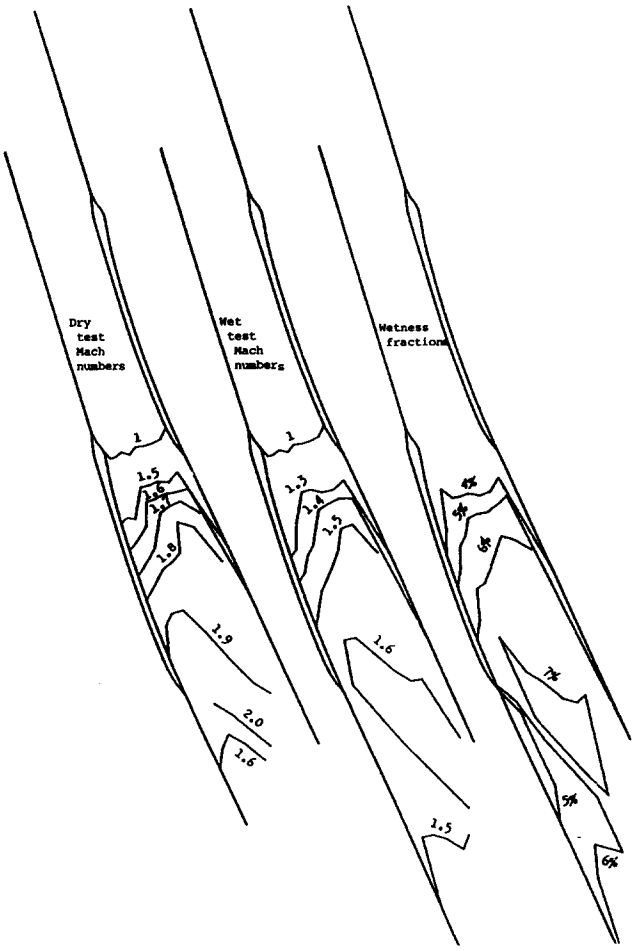

Figure 5 Results of solution 2

supercooling of the fluid is depleted. Beyond this there is a gradual increase in the droplet sizes except in the vicinity of shocks where there is a temporary reduction. Beyond this the droplets continue to grow as the fluid expands. Supercooling of the flow is plotted as positive in Figure 6. Thus the negative supercooling indicates superheating of the steam, which occurs downstream of the shocks.

Schlieren photographs

In addition to the pressure measurements, some Schlieren observations of the flow were also recorded. The photographs of the nucleating flows show a dark line, as indicated schematically in Figure 7, which is absent from those of the dry flows. To investigate whether this line has resulted from a consequence of nucleation and phase change, the zone of rapid condensation in the theoretical results has been identified. The pressure distributions of the dry and wet flows obtained in solution 2 are plotted as a function of the distance along the quasi-streamlines in Figure 8. The pitchwise position of the quasi-streamlines is indicated by the numbers on the curves. The dotted line across the curves corresponds with the end of nucleation in the theoretical solution. The position of the dark line is also superimposed on Figure 8. The agreement between the predicted nucleation zone and the dark line is acceptable. But the theoretical solutions indicate a gradual change in pressure, while dark lines in Schlieren photographs are associated with sudden rises in pressure. A possible explanation might be that the time-marching method smears the changes in the flow.

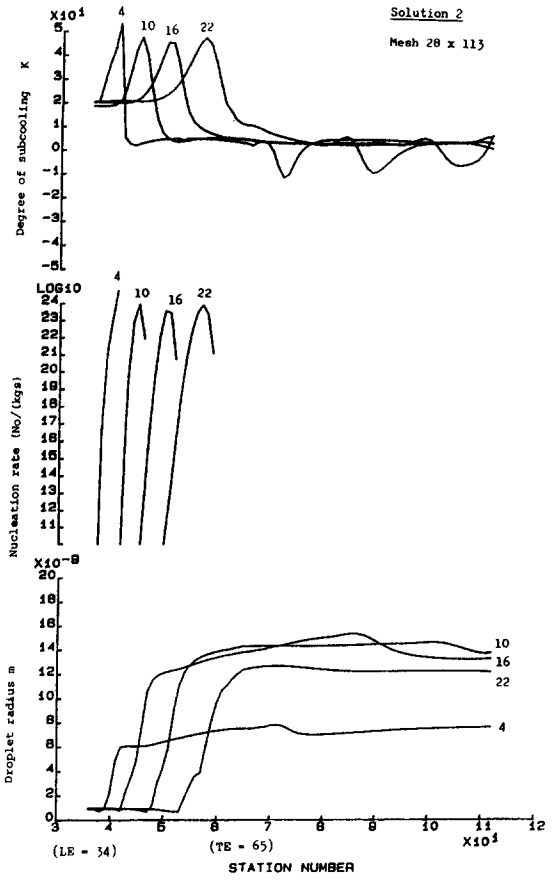

Figure 6 Variations of droplet sizes and nucleation characteristics in solution 2

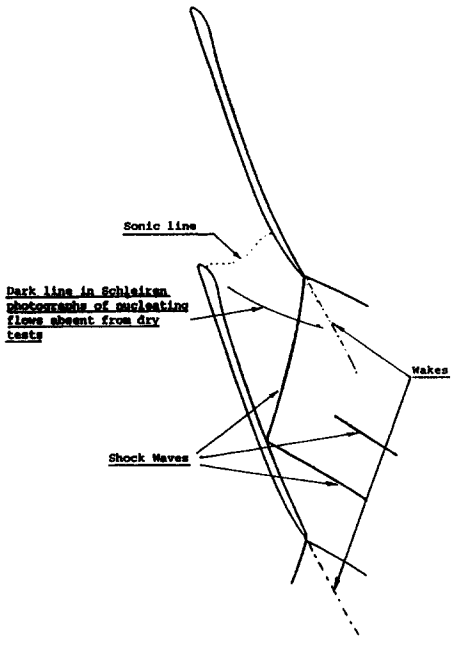

Figure 7 General features of Schlieren photographs

It is known from experimental observations in convergent–divergent nozzles that in supersonic flows, the heat release due to condensation is generally associated with a rise in pressure. Although these pressure changes are sometimes referred to as condensation shocks, the term is misleading. Usually, the changes appear as knees in pressure distributions, and the steepness depends on local conditions. Should such a rise have been sufficiently steep in the flow to show up as a dark line, it would have been smeared in the theoretical solution. To investigate the problem further, the method of solution was applied to the flow in a convergent–divergent nozzle where, from the pressure traverses taken, a small but relatively steep pressure rise has been observed in the zone of rapid condensation. The nozzle was one with a curved throat, with a throat width of 24.87 mm and an angle of divergence of 12°. The steam stagnation conditions were 1.478 bar and 399.2 K. The comparison between the theoretical pressure distribution along the nozzle axis and the experimental observations is shown as an inset to Figure 8.

It can be seen that a small but relatively steep pressure rise has occurred in the nozzle, which is the result of subcritical heat addition that is smeared in the theoretical solution. The inviscid 2-D treatment has predicted the zone of condensation reasonably well but not the pressure rise.

In the case of the flow in the cascade, it is very likely that the dark line is caused by the heat release in the rapid condensation zone, but any pressure change associated with it is smeared in the solution. The discrepancy in the location of the condensation zone can be in part attributed to boundary-layer and base-pressure effects not included in the theoretical treatment.

Wetness losses

The losses resulting from the formation and behavior of the liquid phase in wet steam can be divided into three categories:

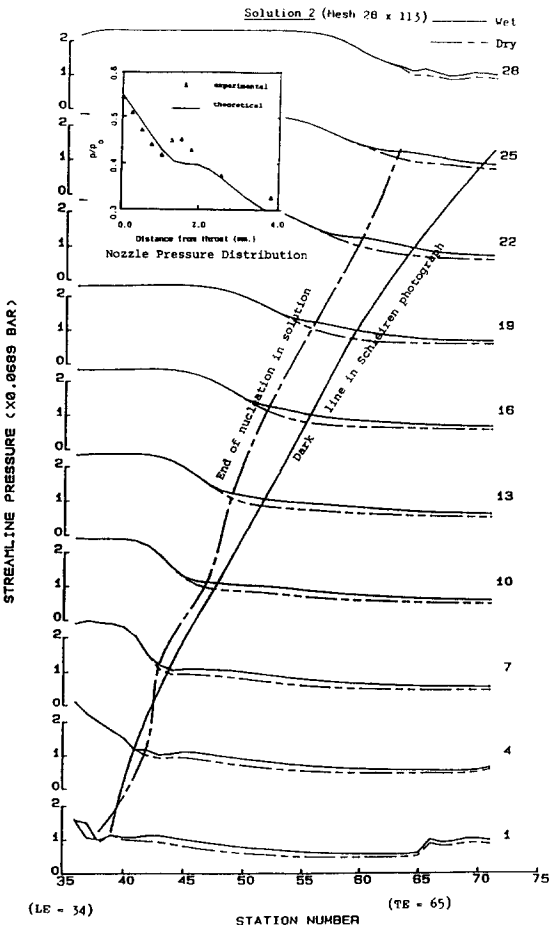

Figure 8 Comparison of position of dark Schlieren line with cascade pressure distribution

mechanical, thermodynamic, and aerodynamic. In the present case the only mechanical effect is the drag of the droplets. Because of the smallness of the droplets, this was assumed to be very small.

Thermodynamic losses. These losses are incurred due to internal heat transfer within the fluid. In the cases of droplet growth the condensing molecules give up latent heat to the droplets, but the bulk of this energy has to be transferred to the vapor. For this purpose a temperature difference will develop between the phases, and the flow of heat across it is thermodynamically irreversible. In cases of evaporation the droplets will have to receive heat from the surrounding vapor. Once again a temperature difference will develop within the fluid, and the flow of heat across it will be irreversible.

In the absence of numerical errors, the increase in entropy resulting from these processes could be obtained directly from the solutions. Because of this difficulty the increase in entropy has been estimated by integrating along the quasi-streamlines. In the case of solution (2) this was estimated to be 4.0% of the isentropic heat drop.

Aerodynamic losses. The influence of two-phase effects on the boundary-layer losses has not been examined. In particular, if the dark line in the Schleiren photograph indicates a pressure rise across the passage, it would have the consequence of increasing the boundary-layer loss. In addition, because of the differences in the thermodynamic paths of the streams reaching the trailing edge from the pressure and suction surfaces, the variation in velocity across the passage is considerable. Disregarding the presence of the wake, the effect of the velocity difference across the passage will be experienced as a mixing loss. Approximate calculations yield a value of 0.8% for this loss. Thus from the present solution, the thermodynamic and mixing components of the wetness loss are estimated at 4.8%. To this must be added the boundary-layer effects, which are as yet undetermined. This is compatible with Ikeda and Suzuki's[6] observations of 8% as the wetness loss in a convergent–divergent nozzle.

Discussion and conclusions

Two-dimensional two-phase flows of steam can be treated by the time-marching method. The supersonic tip section geometry investigated represents a particularly severe test for the calculation method. Despite the presence of a shock wave and very high rates of change of fluid properties in the two-phase region, apart from increasing the need for computing capacity, the droplet growth sequences have presented no particular difficulties.

Because of the sensitivity of nucleating and wet steam flows to the vapor temperature, the accumulated numerical errors associated with the method of treatment can lead to inaccuracies in the solutions, and the quality or value of the results will depend on the extent to which the errors can be avoided or tolerated. It has been demonstrated that a finer mesh can be embedded into selected regions of the basic computational grid and its coordinates transformed if necessary. This increases the capability of the basic technique by increasing the accuracy in the selected region without an undue increase in the overall computing needs.

The degree of agreement between the theoretical solutions and the very limited amount of experimental data available is fair. The calculations predict the surface pressure distributions and the location of the condensation zone reasonably well. But any pressure rise in the zone of rapid condensation resulting from the heat release is smeared in the theoretical solutions. Nevertheless the solutions can still be of value in the interpretation of experimental results. But clearly to obtain more accurate solutions some further refinement of the treatment will be necessary. The use of more accurate algorithms or an embedded grid in the condensation zone are possibilities that remain to be explored.

Two-phase flows are always associated with some thermodynamic loss because of the presence of internal heat transfer during phase change, which is not experienced in dry flows. This is particularly significant when the fluid nucleates. In addition it is expected that further aerodynamic effects, such as boundary-layer losses, can result from phase changes that have not been considered in the present investigation, and further work on the subject is necessary.

Acknowledgments

The investigations reported in this article were carried out in the Mechanical Engineering Department of Birmingham University. The work was supported by the Science and Engineering Research Council.

References

1 Bakhtar, F. and Al-ubaidy, A. K. On the solution of supersonic blade to blade flows of nucleating steam by the time-marching method. *Proc. Inst. Mech. Eng. Conf. on Comput. Method. in Turbomachinery*. I. Mech. E. conference publications, 1984, **3**, C82/84

2 Denton, J. D. A time-marching method for two- and three-dimensional blade to blade flows. ARC R & M 3775, 1975

3 Bakhtar, F. and Mohammadi Tochai M. T. An investigation into two dimensional flows of nucleating and wet steam by the time-marching method. *Int. J. Heat and Fluid Flow*, 1980, **2**(1), 5–18

4 Denton, J. D. An improved time-marching method for turbomachinery flow calculation. 1982, ASME Paper 82-GT-239

5 Yousif, F. H., Campbell, B. A., and Bakhtar, F. Instability in condensing flow of steam. *Proc. I. Mech. Eng.*, 1972, **186**, 37–72

6 Ikeda, T. and Suzuki, A. Some findings on the flow behaviour of last-stage turbine buckets by linear cascade tests in steam. *Proc. I. Mech. Eng. Conf. on Heat and Fluid Flow in Steam and Gas Turbine Plant*, Warwick University, 1973, C26/73, 45–55

Appendix 1: Outline of theoretical treatment

Governing equations

Considering nonsteady, inviscid, 2-D flow of a vapor carrying a monodisperse population of spherical droplets with no interphase slip, the conservation equations of mass, momentum, and energy applied to a finite volume element in the xy rectangular coordinate system together with the state equation may be written as follows.

Mass continuity

$$\Delta t \sum \rho u \, ds_x + \rho v \, ds_y = \Delta V \Delta \rho \qquad \text{(A.1)}$$

where u and v are the velocity components in the x and y directions, ρ is the overall (vapor and liquid) density of the mixture, ΔV is the volume of the element, ds_x and ds_y are the projections of the control volume faces in the x and y directions, respectively, Δt is the time increment, and the summation is made over the faces of the element.

Momentum in the x direction

$$\Delta t \sum (p+\rho u^2)\, ds_x + \rho uv\, ds_y = \Delta V \Delta(\rho u) \tag{A.2}$$

where p is the pressure of the vapor phase.

Momentum in the y direction

$$\Delta t \sum \rho uv\, ds_x + (p+\rho v^2)\, ds_y = \Delta V \Delta(\rho v) \tag{A.3}$$

Energy

Since the steady-state solution is of interest, it is assumed that the flow takes place with constant total enthalpy, and the energy equation is written as:

$$h_o = h + \frac{u^2+v^2}{2} \tag{A.4}$$

where h is the specific enthalpy of the mixture.

Equation of state for the vapor phase

To use mutually consistent thermodynamic properties, it is convenient to adopt a virial equation of state for the vapor phase:

$$p = \rho_G R T_G (1 + B\rho_G) \tag{A.5}$$

where ρ_G, T_G, R, and B are the vapor density, temperature gas constant, and second virial coefficient, respectively.

Two-phase effects

The general Equations A.1–A.5 are applicable to single- or two-phase flows without alteration. In the latter case the only requirement is that the terms ρ and h refer to the overall density and enthalpy of the (liquid plus vapor) mixture. In the case of two-phase flows, the most important influence of phase change is the release of latent heat, which affects the energy equation directly. To deal with two-phase effects, the wetness fraction, w, is introduced into the equations:

$$w = \tfrac{4}{3}\pi r^3 \rho_L N \tag{A.6}$$

where ρ_L is the liquid density; r and N are the mean droplet radius and the number per unit mass of the fluid, respectively, and are calculated from considerations of nucleation and droplet growth. The procedure is described in Appendix 1 of Reference 3. The number of droplets at the end of the calculating step is the sum of those existing in the fluid at the start of the step and the additional ones nucleated over the interval. With the wetness fraction known the mixture enthalpy and density may be written as:

$$h = (1-w)h_G + wh_L \tag{A.7}$$

$$\rho = \frac{\rho_G}{1-w} \tag{A.8}$$

where the subscripts G and L refer to the vapor and liquid phases, respectively.

In combination with the equations governing droplet formation and growth rates, the above equations are sufficient to describe the flow completely. In steady-state flow when the correct values of the flow and fluid properties are substituted in Equations A.1–A.3 the changes in their values with time will become zero. Thus starting with estimated values of the properties, the equations can be integrated forward in time until the steady-state solution has been obtained.

Numerical procedure

With reference to the typical calculation element in the grid system shown in Figure A.1, and using PR to denote any of the flow properties ρ, ρu, and ρv, its changes for the element ABCD are obtained from the conservation equations. With the changes in flow properties of the elements ABCD and ADEF known, its distribution to the calculating points depends on the scheme employed. A common procedure in the time-marching calculations is to assume that changes in flow properties other than pressure act downstream. But to improve the stability of the solution, some smoothing is introduced. Thus the new values of the properties at the time $t+\Delta t$ for a typical point are found from:

$$(PR)_D^{t+\Delta t} = (1-SF_y)(PR)_D^t + \frac{SF_y}{2}(PR_C^t + PR_E^t) + \tfrac{1}{2}(\Delta PR)_{ABCD} + (\Delta PR)_{ADEF} \tag{A.9}$$

where SF_y is the smoothing factor in the y direction.

The actual sequence in which the new values of the flow variables are calculated is as follows:

(1) The density is updated at each point from the continuity Equation A.2.
(2) The pressure is updated at each point from the energy equation using the new value of density and old values of u and v. In regions where the fluid is dry, the calculation is carried out by noting that $\rho_G = \rho$. An initial value is estimated for T_G and the corresponding values of p and h_G calculated. If this value of h_G does not satisfy Equation A.4 to the desired degree of accuracy, a new value of T_G is tried by using the Newton–Raphson method.

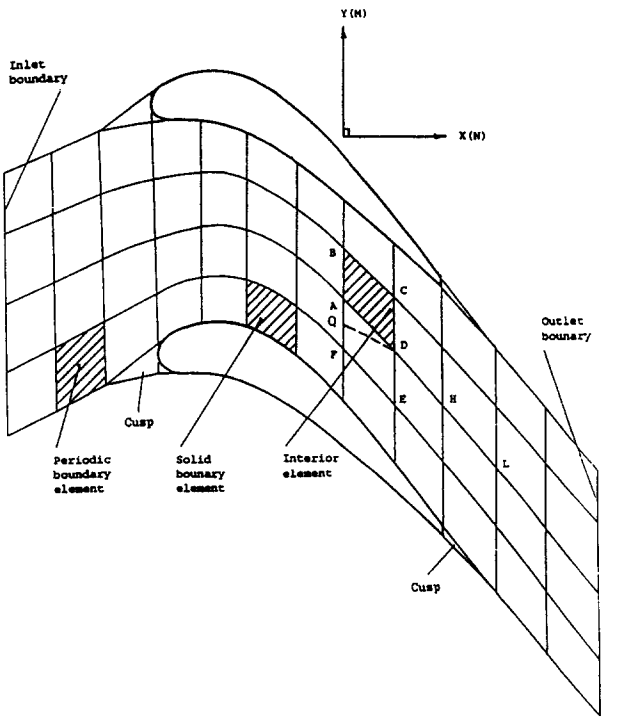

Figure A.1 Grid system

In zones where the flow is nucleating or wet, the procedure is more difficult as Equations A5–A8 have to be satisfied simultaneously with equations describing droplet nucleation and growth. With reference to Figure A.1, for this purpose point Q is identified along AB to lie along the streamline passing through D and the conditions at Q calculated by linear interpolation between the two points on either side of it along the station. With the conditions at Q determined, the values of droplet radius r_Q and number per unit mass N_Q at this point are adopted as the starting conditions for the calculation of droplet growth rate along QD. At the end of the calculation if the resulting liquid terms do not match the estimated conditions at D, new estimates are formed and the procedure repeated.

(3) ρu is updated at each point from Equation A.2 using old values of ρ, u, and v and the new upwinded value of pressure (p_D). This value of pressure is for substitution into the momentum equation only, and its determination depends on the calculation scheme employed. In the present study the scheme adopted is that described as scheme C by Denton[3] in which (ρ_D) is calculated from the new density at the next downstream point plus a density correction factor. For a perfect gas,

$$p_D = (\rho_H + CF_{\rho D})RT_D \tag{A.10}$$

(4) ρv is updated from Equation A.3 using old values of ρ, u, and v and the new value of p.

(5) New values of u and v are obtained from new values of ρu, ρv, and ρ.

(6) With reference to Figure A.1, new density correction factors are calculated for all the calculating points from:

$$(CF_{\rho D})^{t+\Delta t} = (1-RF)(CF_\rho)^t_D + RF(1-f)(1-G)(\rho_D^{t+\Delta t} - \rho_H^{t+\Delta t}) + \tfrac{1}{3}G(\rho_A^{t+\Delta t} - \rho_H^{t+\Delta t}) \tag{A.11}$$

where RF is the relaxation factor, f is termed the residual down winding pressure by Denton and provides some numerical damping in the solution, and G is a factor to introduce second-order corrections into the solution.

The maximum value of the time-step Δt_m is chosen as:

$$\Delta t_m = FT\frac{\Delta x_{min}}{c_o}$$

where Δx_{min} is the shortest axial spacing in the grid, c_o, is the speed of sound under upstream stagnation conditions, and FT is a time factor smaller than unity.

Appendix 2: Embedded grid arrangement and calculation procedure

Arrangement of mesh

With reference to Figure 1b, it will be seen that it is difficult to model accurately the flow around the blade nose with the standard grid. The problem may be greatly eased if the flow field can be divided into two zones: the main field and that in the special zone. Points A_1, A_2, C_7, H_2, H_1, E_2, E_1, and C_8 are boundary points common to both fields. The main flow field is covered by the main grid outside this zone as before, but its boundary with the blade surface is replaced by its interaction with the flow in the small zone.

The flow in the special zone is bounded by surface E_2, E_1, C_8, A_1, A_2, C_7, H_2, and $H_1$and interacts with the main flow and H_1, D_2, and E_2, which represents the surface of the blade. This section of the field can be covered by a separate mesh embedded in the main grid. Furthermore, by careful selection of the mesh increments, the quasi-orthogonals of the embedded mesh can be made perpendicular to the inlet flow direction. In the arrangement shown in Figure 1b, the blocks of the embedded grid are formed by the intersections of the broken lines. Except for the common lines between the two grids, the remainder of the grid lines of the main mesh are shown by full lines. It is also seen that, to facilitate transfer of information between the two grids without the need for interpolation, it is possible to arrange the calculating points to be common to both grids.

With the overall features of the embedded mesh determined, the coordinates of the embedded grid can be transformed and the positions of the common calculating points and vector properties of the flow transformed into the new coordinates. At this stage, as shown in Figure A.2, the blocks of the embedded grid can be further subdivided into a finer mesh if desired.

Numerical procedure

A typical example of an embedded grid used in the investigation is shown in Figure A.2. It will be noted that with this arrangement the blade shape can be represented more accurately. Points a_3, b_3, c_3, h_3, a_{10}, b_{10}, and e_{10} are common to both grids. Points b_3, c_3, b_{10}, and c_{10} are typical calculating points of the embedded grid, while points a_2, a_4, and a_{17} are intermediate between the calculating points to the main mesh.

The basic numerical procedures are the same as those used

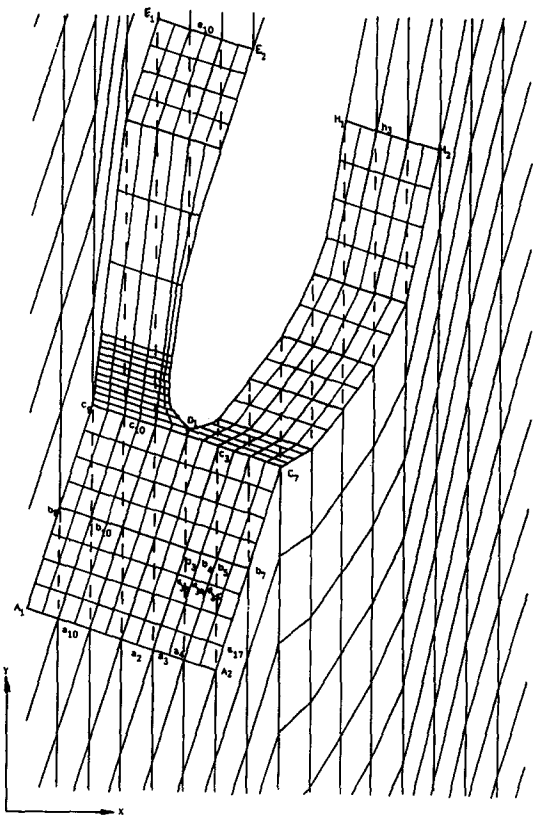

Figure A.2 Arrangement of embedded grid

for the main mesh. Using b_4 as an example, the flow properties ρ, ρu, and ρv denoted as PR are updated as:

$$PR_{b4}^{t+\Delta t} = PR_{b4}^{t} + \tfrac{1}{2}(\Delta PR_{a_{35}b_5b_4a_{34}} + \Delta PR_{a_{34}b_4b_3a_{33}}) \qquad (A.12)$$

The use of Equation A.12 for the evaluation of the flow properties at the calculating points depends on whether or not they lie on the corners of elements. Taking points a_2 and a_{17} as examples of those that do not lie on the corners of elements, the corresponding flow properties are obtained by interpolation between a_2 and b_7. Calculating points common to both grids can be divided into two groups. The first group is typified by b_3 and b_5. For the purposes of updating, they are treated the same as other points in the embedded mesh. But the updated properties are transformed vectorially before entering in the main mesh. The second group is typified by b_7, c_7, b_8, and c_8, which are on the boundary between the two zones. The properties at these points are updated in the main grid. They are then transformed before use in the embedded mesh. The remainder of the calculating points of the embedded mesh that are not common to both grids are updated normally.